Geophysical Research Letters

RESEARCH LETTER
10.1029/2021GL095895

Special Section:
ExoMars Trace Gas Orbiter - One Martian Year of Science

First Detection and Thermal Characterization of Terminator CO_2 Ice Clouds With ExoMars/NOMAD

Giuliano Liuzzi[1,2], Geronimo L. Villanueva[1], Loïc Trompet[3], Matteo M. J. Crismani[4], Arianna Piccialli[3], Shohei Aoki[3,5,6], Miguel Angel Lopez-Valverde[7], Aurélien Stolzenbach[7], Frank Daerden[3], Lori Neary[3], Michael D. Smith[1], Manish R. Patel[8], Stephen R. Lewis[8], R. Todd Clancy[9], Ian R. Thomas[3], Bojan Ristic[3], Giancarlo Bellucci[10], Jose-Juan Lopez-Moreno[7], and Ann Carine Vandaele[3]

[1]NASA Goddard Space Flight Center, Greenbelt, MD, USA, [2]Department of Physics, American University, Washington, DC, USA, [3]Royal Belgian Institute for Space Aeronomy, BIRA-IASB, Brussels, Belgium, [4]California State University San Bernardino, San Bernardino, CA, USA, [5]LPAP, STAR Institute, Université de Liège, Liège, Belgium, [6]Institute of Space and Astronautical Science (ISAS), Japan Aerospace Exploration Agency (JAXA), Sagamihara, Japan, [7]Instituto de Astrofisica de Andalucia, IAA-CSIC, Glorieta de la Astronomia, Granada, Spain, [8]School of Physical Sciences, The Open University, Milton Keynes, UK, [9]Space Science Institute, Bald Head Island, NC, USA, [10]Istituto di Astrofisica e Planetologia Spaziali, IAPS-INAF, Rome, Italy

Abstract We present observations of terminator CO_2 ice clouds events in three groups: Equatorial dawn, Equatorial dusk (both between 20°S and 20°N) and Southern midlatitudes at dawn (45°S and 55°S east of Hellas Basin) with ESA ExoMars Trace Gas Orbiter's Nadir and Occultation for MArs Discovery instrument. CO_2 ice abundance is retrieved simultaneously with water ice, dust, and particle sizes, and rotational temperature and CO_2 column profiles in 16 of 26 cases. Small particles (<0.5 μm) prevail at dusk, while water ice likely provides most source nuclei at dawn. Clouds east of Hellas are found to be dominantly nucleated on surface-lifted dust. CO_2 ice is sometimes detected in unsaturated air together with dust nuclei at dawn, suggesting ongoing sublimation. Depending on latitude and local time, the interplay between particle precipitation and the lifetime of temperature minima (i.e., cold pockets) determines CO_2 ice properties.

Plain Language Summary The upper atmosphere of Mars is characterized by the seasonal presence of CO_2 ice clouds. Their properties have been long studied, as well as their formation mechanisms in relation to the thermal structure of the atmosphere and its variability. In this study, we present the first observations of these clouds at the terminator (dawn and dusk) by the NOMAD spectrometer onboard the Exomars Trace Gas Orbiter. CO_2 ice is detected simultaneously with dust, water ice and the temperature profile. Our results agree with previous findings in terms of how clouds are spatially distributed and their temporal occurrence. However, we also explore the sources of condensation nuclei for CO_2 ice particles, showing that water ice is a possible source at dawn near the Equator. We also identify surface-lifted dust below the CO_2 ice clouds observed east of Hellas Basin, suggesting that, at that location, dust could provide nuclei for CO_2 ice. CO_2 ice is also sometimes detected at temperatures higher than the CO_2 freezing point, suggesting ongoing sublimation. In this work we explore for the first time the composition of CO_2 ice clouds, which is critical to advance our understanding of how CO_2 ice clouds form in the mesosphere at Mars.

Key Points:

- Twenty Six mesospheric CO_2 ice clouds were detected with NOMAD SO in Mars Year 35, simultaneously with water ice, dust, and CO_2 saturation ratios
- Equatorial CO_2 clouds are observed at 50–80 km altitude at dusk, and 40–60 km at dawn, when water ice likely provides condensation nuclei
- Six CO_2 ice clouds are found east of Hellas basin; their formation is likely sourced by surface-lifted dust at 40–65 km

Supporting Information:

Supporting Information may be found in the online version of this article.

Correspondence to:

G. Liuzzi,
giuliano.liuzzi@nasa.gov

Citation:

Liuzzi, G., Villanueva, G. L., Trompet, L., Crismani, M. M. J., Piccialli, A., Aoki, S., et al. (2021). First detection and thermal characterization of terminator CO_2 ice clouds with ExoMars/NOMAD. *Geophysical Research Letters*, *48*, e2021GL095895. https://doi.org/10.1029/2021GL095895

Received 2 SEP 2021
Accepted 27 OCT 2021

Author Contributions:

Conceptualization: Giuliano Liuzzi
Data curation: Giuliano Liuzzi, Bojan Ristic
Formal analysis: Giuliano Liuzzi, R. Todd Clancy

1. Introduction

CO_2 ice clouds are unique features of Mars' atmosphere, occurring often around aphelion and in polar nights. Conditions for CO_2 condensation were first observed during the Pathfinder descent (Schofield et al., 1997) around 80 km, and CO_2 ice cloud formation has been discussed in multiple works. Clancy and Sandor (1998) and Magalhães et al. (1999) showed that CO_2 can condense in supersaturated air pockets formed by constructive interference of thermal tides and/or gravity waves. González-Galindo et al. (2011) determined that mesospheric CO_2 ice clouds form in temperature minima due to atmospheric thermal tides, even where the temperature is not low enough to cause condensation. Wherever gravity waves do

Funding acquisition: Geronimo L. Villanueva
Investigation: Giuliano Liuzzi, Geronimo L. Villanueva, Loïc Trompet, Matteo M. J. Crismani, Arianna Piccialli, Shohei Aoki, Miguel Angel Lopez-Valverde, Frank Daerden, Lori Neary, Michael D. Smith, Manish R. Patel, R. Todd Clancy, Ann Carine Vandaele
Methodology: Giuliano Liuzzi, Geronimo L. Villanueva
Project Administration: Ann Carine Vandaele
Software: Giuliano Liuzzi, Geronimo L. Villanueva
Supervision: Geronimo L. Villanueva
Validation: Giuliano Liuzzi, Loïc Trompet, Matteo M. J. Crismani, Arianna Piccialli, Shohei Aoki, Miguel Angel Lopez-Valverde, Aurélien Stolzenbach, Manish R. Patel, R. Todd Clancy
Visualization: Giuliano Liuzzi, Geronimo L. Villanueva, Matteo M. J. Crismani, Michael D. Smith
Writing – original draft: Giuliano Liuzzi
Writing – review & editing: Giuliano Liuzzi, Geronimo L. Villanueva, Loïc Trompet, Matteo M. J. Crismani, Arianna Piccialli, Shohei Aoki, Miguel Angel Lopez-Valverde, Aurélien Stolzenbach, Frank Daerden, Lori Neary, Michael D. Smith, Manish R. Patel, Stephen R. Lewis, R. Todd Clancy, Ian R. Thomas, Ann Carine Vandaele

not destructively interfere and can propagate upward into the mesosphere, CO_2 is likely to condense (Spiga et al., 2012). Simulations with temperature profiles that take these dynamics into account (Listowski et al., 2014) produced mesospheric CO_2 ice clouds that are consistent with the observed locations and times.

CO_2 mesospheric clouds have been characterized with several space-based observations, as they are effective tracers of thermal tides and gravity wave propagation in the upper atmosphere. The first detection was claimed using Mariner and Pathfinder descent data (Clancy & Sandor, 1998) arguing that such clouds would form in the low latitude mesosphere with tidal- and gravity wave-induced temperature minima, but subsequently the observation of diffuse CO_2 fluorescence questioned the Mariner discovery (Piccialli et al., 2016). The first systematic study of their distribution was performed with MGS-TES data and MOC limb data (Clancy et al., 2004, 2007) over the course of Mars Years (MY) 24–26 at specific local times (13–15 hr). These results showed that mesospheric clouds occur at altitudes of 70 km, latitude 10°S to 10°N and longitude 20°E to 20°W, 70 to 110°W, mostly at $L_S = 20–35°$ and 145–160°. The first nighttime CO_2 ice clouds were observed at altitudes 80–110 km, at low to mid S latitudes and $L_S = 134–137°$ using UV stellar occultations by SPICAM on board Mars Express (MEx) (Montmessin et al., 2006). This is also the first case of simultaneous identification of CO_2 ice absorption and atmospheric temperature (also in Jiang et al., 2019), which unambiguously classified the observed absorption as CO_2 ice as opposed to water ice.

A global view of mesospheric CO_2 ice daytime clouds was provided by the MEx-OMEGA, and the CRISM onboard the Mars Reconnaissance Orbiter (MRO) (Clancy et al., 2019; Määttänen et al., 2010; Montmessin et al., 2007; Vincendon et al., 2011). In MY 27–29, 60 occurrences of daytime mesospheric CO_2 clouds were found in OMEGA data (Määttänen et al., 2010), from $L_S = 0–120°$, with an interruption at $L_S = 60–90°$. Most of the observations occurred at low latitudes and altitudes 60–85 km, with only three exceptions at southern mid-latitudes (−45 to −49°S) at lower altitudes (53–62 km). CO_2 ice clouds have been detected in specific longitudinal corridors (Spiga et al., 2012) around Sinus Meridiani and Valles Marineris, suggesting that diurnal thermal tides play a role in CO_2 ice formation.

The spatial and temporal distributions of CO_2 cloud detections by OMEGA and CRISM were confirmed by an independent analysis using PFS-MEx (Aoki et al., 2018), which showed 111 CO_2 clouds detections in MY 27–32. The high spectral resolution of PFS allowed to test the accuracy of different sets of refractive indices to reproduce CO_2 ice extinction (Warren, 1986; Wood & Roux, 1982) at 4.2 μm. This investigation indicated the need to further improve the characterization of CO_2 ice optical properties and their dependencies on particle shape, which varies with temperature. Particle sizes derived with PFS and OMEGA fell in the range 1–3 μm, with an average radius of 2.2 μm. The study by Clancy et al. (2019) showed unique vertical and spatial distributions of particle size and new diagnostic information on size distribution variances, particularly the very narrow distribution associated with iridescence in many CO_2 clouds, and particles as small as 0.3 μm in daytime. Unexpectedly much larger particles (up to 7 μm) occurred at night, suggesting that high-altitude atmospheric updrafts could be strong enough to counteract the fast gravitational precipitation (>10 m/s) of particles (Montmessin et al., 2007).

Observations of CO_2 ice clouds at the terminator should place important constraints on existing working hypotheses about their formation and lifetime: the current understanding comes primarily from measurements taken at two local times, centered around 2–3 a.m./p.m., with limited evidence of their properties at other local times. Some useful observations have been provided by Stevens et al. (2017), where 161 mesospheric clouds were observed at 5–11 a.m. by the Mars Atmosphere and Volatile EvolutioN (MAVEN) IUVS spectrograph during MY33. Many of these clouds were located at tangent altitudes 60–80 km near −110°E, −10°E and 90°E near the Equator. Although these measurements could not distinguish water ice from CO_2 ice, IUVS data showed a coupling between upper atmospheric temperature oscillations due to thermal tides enabling the formation of mesospheric clouds.

This work explores the connection between mesospheric CO_2 ice clouds, temperature, dust, and water ice at the terminator. Although no daily contiguous latitudinal coverage can be obtained (Neefs et al., 2015; Thomas et al., 2016), NOMAD data have contributed to build a global view of aerosols (Liuzzi et al., 2020), and here are used to map CO_2 ice clouds simultaneously with dust, water ice, their particle sizes, as well as to estimate the vertical temperature profile to identify CO_2 supersaturation. This latter aspect is relevant to understanding whether the formation of cold air pockets occurs at locations differing from previous

measurements, to inform the role of thermal tides and gravity waves (e.g., Yiğit et al. (2015)), whether CO_2 ice is detected coincidentally with thermal minima, and to formulate hypotheses about CO_2 ice lifetime in the atmosphere.

2. Data, Methods, and Uncertainties

NOMAD is part of the payload of ExoMars Trace Gas Orbiter 2016, an ESA/ROSCOSMOS mission to Mars. In this work we use the data from the Solar Occultation channel of NOMAD, SO, whose science observations started in April 2018. This operates in the IR (2.2–4.3 μm, 2325-4500 cm^{-1}) with a spectral resolving power close to 20,000. SO consists of an echelle grating in a Littrow configuration combined with an Acousto-Optic Tunable Filter (AOTF) that selects the diffraction orders of interest. Each measurement consists of a cycle of five or six diffraction orders, chosen to include absorption by gases/organics of interest. As SO is pointed toward the Sun, it observes the solar radiation attenuated by the atmosphere at increasing/decreasing altitudes (dawn/dusk). Each measurement has vertical sampling of 0.6–1.5 km, depending on the angle between surface and line of sight. More details are reported in Liuzzi et al. (2019), Vandaele et al. (2018) and in the Supporting Information S1.

The foundations of the aerosols retrieval methods for SO data are extensively described in Liuzzi et al. (2020). This work slightly adapts these methods to identify CO_2 ice and its specific features. The data used in this study correspond to the level 1.0a of the data provided by the NOMAD PI institute (nomad.aeronomie.be) between Feb/2019 (L_S = 340° MY 34) and Nov/2020 (L_S = 325° MY 35). For each altitude and diffraction order, the data contain the derived atmospheric transmittances from the surface up to the top of atmosphere, used to compute a broadband spectrum by aggregating all the measured orders at each altitude. As demonstrated in Liuzzi et al. (2020) SO data are sensitive to water ice, dust abundances, and to their particle sizes, especially for small water ice particles, while the information content is limited for dust (e.g., Smith et al., 2013).

Because of the similarity between the broadband extinction properties of dust and CO_2 ice the latter would be initially detected as dust using the methods developed so far. This is particularly true around the aphelion, when high altitude dust rarely occurs, except for rocket dust storms in region with enhanced gradients in the topography (Spiga et al., 2013). Therefore, data need additional processing to isolate genuine CO_2 ice detections from dust. In this work this is done both spectrally and by deriving an atmospheric temperature proxy to verify whether it is below the CO_2 freezing point. These two supplementary analyses are performed for any observation where "dust" is detected at L_S = 320-150°, and altitudes >30 km.

The spectral indicator of CO_2 ice is given by characteristic CO_2 ice features (the $2\nu_2 + \nu_3$ and $\nu_1 + \nu_3$ combination bands, respectively centered at 3600 and 3710 cm^{-1}). These features allow to unambiguously distinguish CO_2 ice from dust, and is automatically detected in the spectra when its amplitude exceeds 0.005 over the continuum, with possible false positives that are excluded by visual inspection. The second indicator is provided by atmospheric temperature: consistently with the scheme to retrieve aerosols abundance, we estimate simultaneously the rotational temperature and CO_2 column density along the line of sight using spectra acquired in orders 147 to 149 (3300-3375 cm^{-1}) in the occultations of interest. Each observation is considered independent of the others, similarly to previous works (e.g., Mahieux et al., 2015). Retrievals are performed using the Planetary Spectrum Generator (Villanueva et al., 2018) where the retrieval module is based on Optimal Estimation (OE, Liuzzi et al., 2016; Rodgers, 2000). A-priori information about temperature and CO_2 density is provided by the GEM-Mars model (Neary & Daerden, 2018). Also, since T and CO_2 retrievals are performed only when orders 147 to 149 are observed, CO_2 ice abundance is always reported relative to the density profile as in GEM and not to the retrieved ones, as they are not always available.

An example to showcase the retrieval of CO_2 ice clouds with SO is presented in Figure 1. The analysis of high-resolution radiances is used to confirm that the observed absorption above 40–42 km is due to CO_2 ice. The $\nu_1 + \nu_3$ feature is propagated from order 164 (where is originally located) to order 169 by the AOTF (Liuzzi et al., 2019), and is visible at many altitudes up to 61 km. Further proof of the detection is provided by the rotational temperature proxy, which drops well below the CO_2 freezing point (Sánchez-Lavega et al., 2015) in coincidence with CO_2 ice.

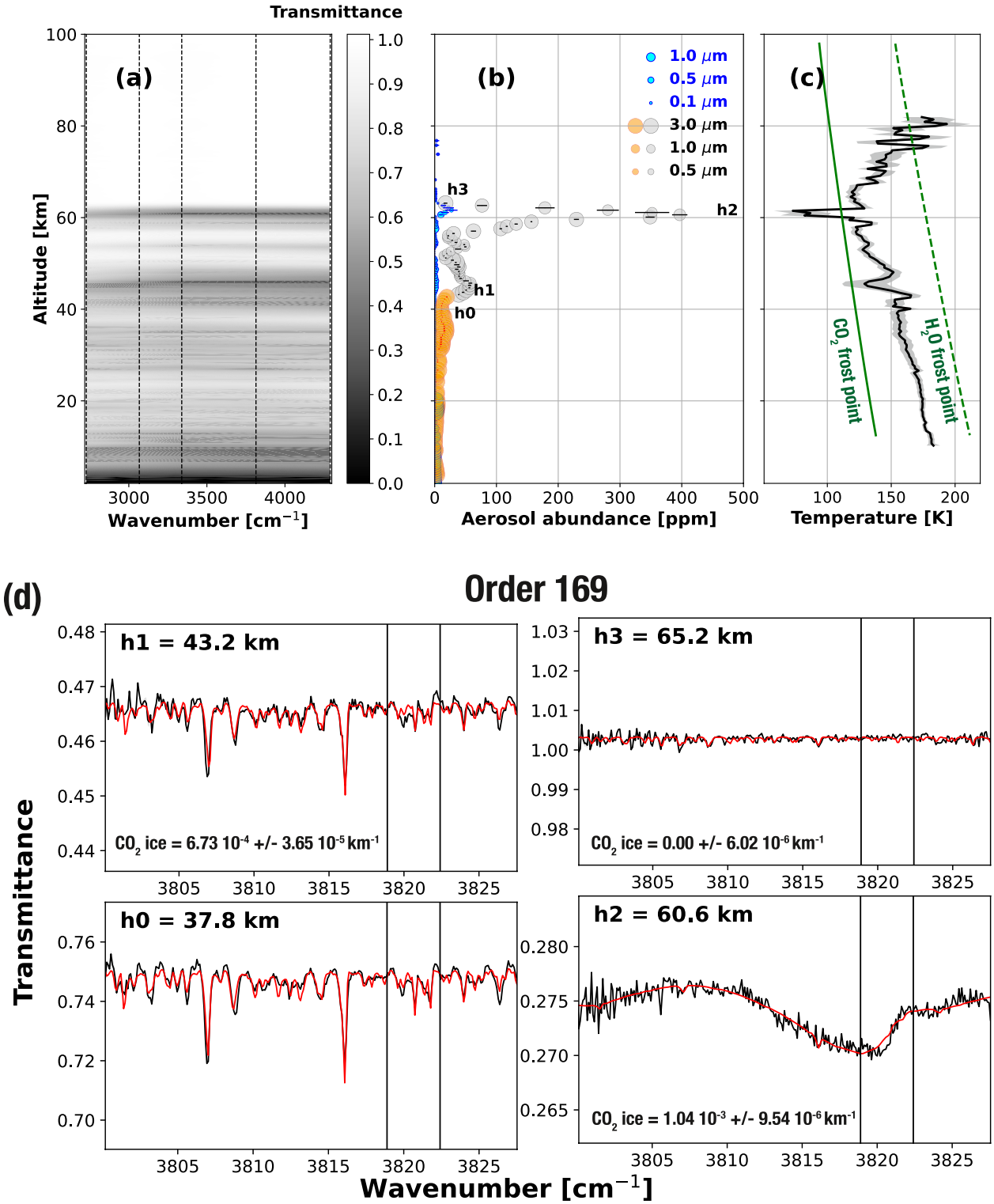

Figure 1. Detection of CO_2 ice during a NOMAD occultation (2019/07/15, 16:35 UTC, Lat 44.7 °S, Lon 146.3 °E, L_S = 53.1°). (a) Continuum transmittance in each order (identified by the vertical lines). (b) Retrieved profiles of water ice (blue), CO_2 ice (black) and dust (orange), and their particle size; (c) derived rotational temperature proxy. (d) Spectra of order 169 at different altitudes (red: fit; black: data). The vertical lines indicate the position where to expect the $\nu_1 + \nu_3$ feature (not included in the fit, except for h2).

The statistical uncertainties derived by the OE on CO_2 ice, dust and water ice opacity are 10%–20%, and are driven by the uncertainty on the broadband transmittances and their fluctuations due to the AOTF function and continuum (Liuzzi et al., 2020). The uncertainty on the particle sizes is usually large for CO_2 ice and dust (>30%). In most cases, basic distinctions can only be drawn between small (<0.5, <1 μm) and large particles (>1 μm). The uncertainty on water ice particle size is smaller because of the strong dependence of spectral shape on particle size: it usually is 0.2–0.4 μm for particles <2 μm, and >0.5 μm for particles >2 μm.

The uncertainties on retrieved temperatures are usually 5–30 K (Mahieux et al., 2015), depending upon the opacity level. However, it must be noted that the retrieved temperature is only a proxy of the local temperature at the tangent height and is not directly obtained by considering hydrostatic equilibrium. Therefore, other effects such as sharp temperature gradients above the tangent height may yield differences between the local temperature and the measured one. The retrieved uncertainty on temperature is smaller than the difference between water and CO_2 frost points, which ranges from 50 to 70 K in average Martian conditions (Sánchez-Lavega et al., 2004), allowing to avoid issues in interpreting the nature of the observed clouds. Retrievals of CO_2 column, which is independent of the temperature are affected by a 5%–20% uncertainty, and are particularly challenging at lower altitudes, where subtleties in the modeling of saturated lines can complicate the estimation of the CO_2 column.

Finally, the retrieved altitude of aerosols is itself affected by an uncertainty, as they could be located higher than the tangent altitude along the line of sight, because occultations are not purely 1-D and can span several degrees in latitude-longitude. This uncertainty can be quantified in 5–10 km and is considered when the correlation between aerosols and temperature is analyzed. Nevertheless, the quantities derived from SO observations have very similar vertical sensitivity, allowing to draw connections between aerosols, their properties, and the temperature proxy. More details on retrievals are given in the Supporting Information S1.

3. Results and Discussion

3.1. Spatial and Temporal Distribution

The sparse nature of TGO measurements—related to its orbital constraints–implies that the detections presented here are not exhaustive of the actual variability of CO_2 ice properties at Mars' terminator. However, SO detections permit comparison with previous results, mostly descriptive of the daytime cloud formation dynamics, and to identify peculiarities of CO_2 ice terminator clouds. Figure 2 shows a summary of the 26 detections and a comparison with some of the most extensive previously published CO_2 clouds databases (Aoki et al., 2018; Stevens et al., 2017; Vincendon et al., 2011). It also shows the frequency of CO_2 ice detections over the total number of observations in the regions of interest identified based on previous works. The location of the SO detections is mostly consistent with daytime clouds, where most of them are located above the Tharsis region (50-120 °W), and in the equatorial region where steep surface elevation gradients occur. Observations confirm that the period of maximum cloud formation activity at the Equator is centered at $L_S = 20°$ (Vincendon et al., 2011). One notable exception is an SO detection of a dawn cloud in MY 35 at $L_S = 320°$ and 52 °N, which is the earliest and northernmost mesospheric CO_2 ice cloud ever detected.

SO detections are vertically resolved, while the altitude of clouds detected in Nadir can be inferred only indirectly by the temperature profile, when available. This is the case of the results in Aoki et al., (2018), where co-located temperature profiles from PFS/MEx suggest that daytime equatorial clouds form at altitudes above 50 km; similar values are reported using independent observations by CRISM (Clancy et al., 2019). SO detections suggest that the altitude of CO_2 ice at the terminator varies, and that while the average altitude of CO_2 ice clouds at the equator is 50–70 km, they are observed at ∼40 km around $L_S = 120°$.

The physical driver of the CO_2 ice cloud variability can be investigated by contextualizing these observations with the simultaneously retrieved dust, water ice, and CO_2 ice particle size profiles. With some exceptions, SO data show the same dichotomy seen in Clancy et al., (2019), where particle radii are <1 μm for dusk clouds, and larger than 2 μm at dawn with sizes up to 5 μm (full list in Supporting Information S1). Overall, CO_2 ice clouds properties vary with location and local time, and the CO_2 ice clouds in this work can be divided in three different groups: (a) Equatorial dusk clouds; (b) Equatorial dawn clouds; (c) "Hellas" dawn clouds.

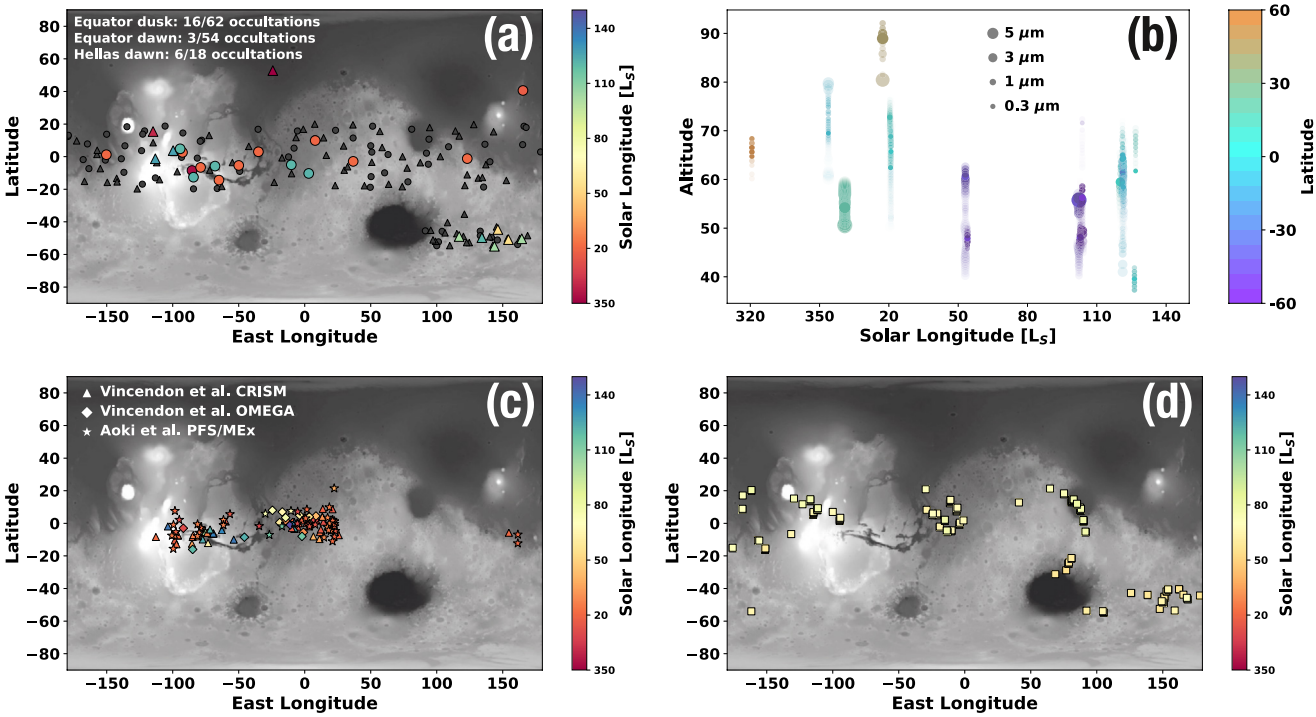

Figure 2. (a) SO CO_2 ice clouds detections map (dawn: triangles; dusk: circles). The color of each detection represents the season (L_S); the dark gray markers indicate all SO observations between L_S 340° MY34 and 325° MY35 in the regions of interest with no CO_2 ice detection. Regions of interest are defined as: (20 °S, 20 °N) × (180 °W, 180 °E) and (60 °S, 40 °S) × (90 °E, 180 °E). (b) SO detections vertical profiles. The opacity of each dot indicates the opacity at each altitude. (c) Same as (a), for previous works (MY 27 to 32) daytime detections; (d) detections of ice clouds (water and/or CO_2) at 5–11 a.m. and >60 km during MY33 in Stevens et al. (2017).

3.2. Equatorial Clouds

Figures 3a-3c show the cases where CO_2 ice was detected with other aerosols and temperature, and figures 3d–3f show the distribution of retrieved particle size against their retrieved number density for the Equatorial and Hellas clouds. Despite SO capability to detect CO_2 ice, in cases where dust and CO_2 ice are present together, SO data cannot unambiguously identify the mixing ratio of both: SO results show only where CO_2 ice is detected, noting that part of the retrieved CO_2 ice may actually be dust, and that the CO_2 ice abundances reported herein constitute an upper limit to the actual abundances. To represent the rotational temperature proxy (see Supporting Information S1) and CO_2 partial pressure profiles cohesively, the aerosol profiles are shown with a derived CO_2 saturation ratio, S (Kasting, 1991; Noguchi et al., 2014). By definition, when S = 1.0, the temperature is the CO_2 condensation temperature at a given pressure (Sánchez-Lavega et al., 2004); however, past modeling efforts have shown that the critical S for the heterogeneous nucleation probability to be unity (i.e., all nuclei are activated within 10^{-3} s) is 1.32–1.35 for CO_2 (Glandorf et al., 2002; Määttänen et al., 2005). Assuming an uncertainty of 5 K on a retrieved temperature that yields S = 1, the confidence interval of S is 0.2–4.6, enabling some considerations on CO_2 ice nucleation for values outside this range.

The equatorial clouds detected by SO are consistent with previous studies (Clancy et al., 2019; Määttänen et al., 2010), that report particle size >1.0 μm in daytime in the primary cloud region, and smaller particles at its margins. Here particles <1.0 μm are often seen, and the particle size characterization is affected by uncertainties of 0.1–0.3 μm. In most cases, particle sizes slightly decrease with altitude, consistently with sedimentation of larger particles, and clouds' vertical extension varies between 15 and 27 km at dusk, a factor of 1.5–3 larger than dawn. SO retrievals indicate that larger CO_2 ice particles occur in the same cases where water ice is more abundant at the same altitudes. For example, this is the case at L_S = 120.2° and 121.6° at dusk, where large (>2.0 μm) water ice particles are observed at altitudes up to 65 km at 80–90 W, and at the same altitude as CO_2 ice. This is when cloud formation in the Aphelion Cloud Belt (ACB)

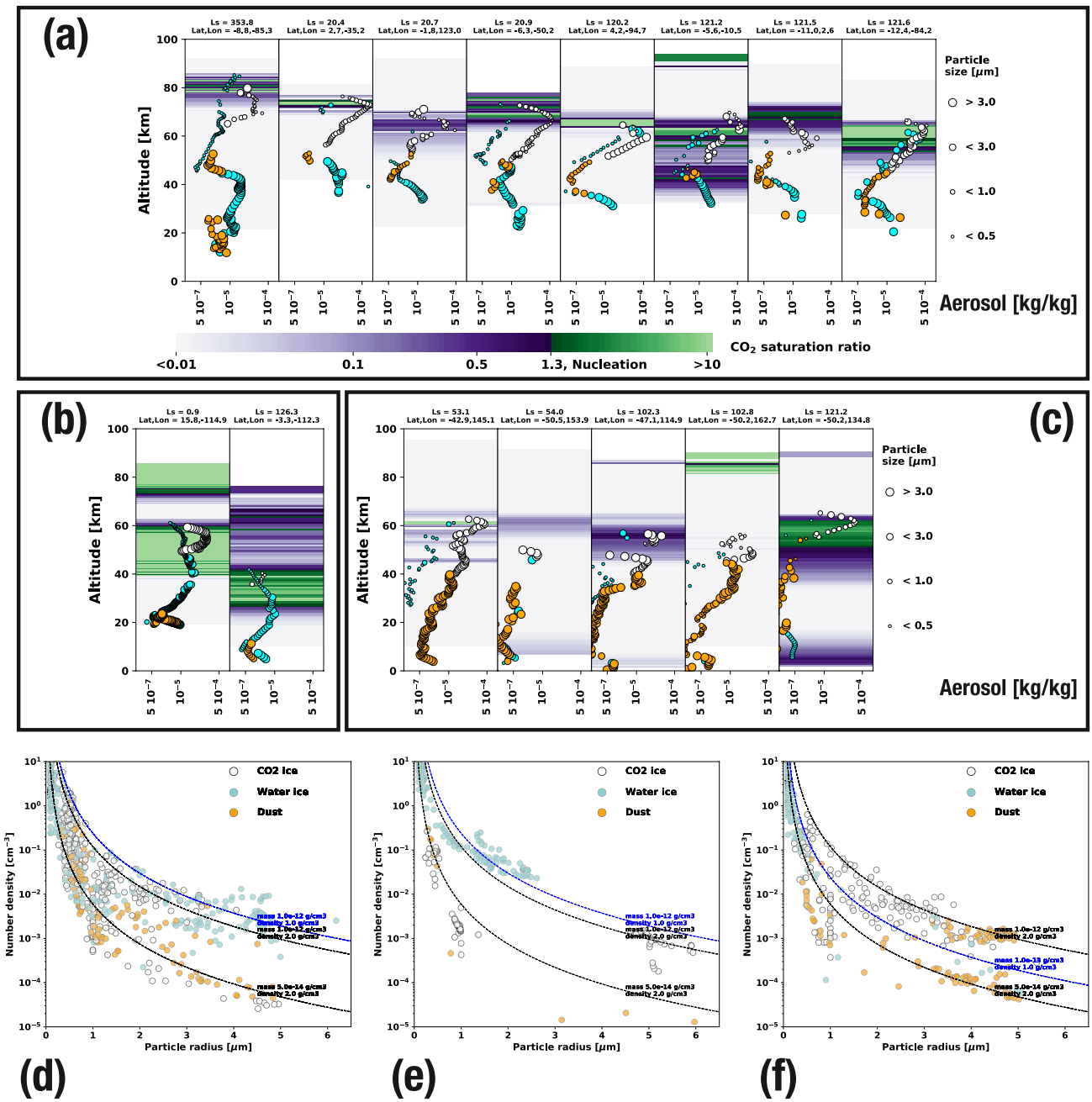

Figure 3. (a) Summary of the detections in the Equatorial region at dusk, dawn (b) and in the Hellas region at dawn (c). The plots report only the cases in which temperature (and CO_2 saturation ratio, contours) is retrieved together with the properties of dust (orange dots), CO_2 ice (white) and water ice (blue). The bottom plots report the particle size versus number density from all the Equator clouds, dusk (d), dawn (e) and Hellas (f), compared to reference constant-mass lines.

is expected to be the most active (e.g., Smith, 2004; Wolff et al., 2019). Previous works (e.g., McCleese et al., 2010; Smith et al., 2013) and current modeling by the Mars Climate Database (Millour et al., 2015) show that water ice is confined mostly below 50 km. These two cases show that sporadic lifting of water ice particles above the ACB cloud top can occur, and previous studies envisaged a similar evolution of the ACB behavior after $L_S = 120°$ (Clancy et al., 1996). Often, surface-lifted dust is detected at the bottom of CO_2 ice clouds, suggesting that dust, and occasionally water ice crystals, may be sources of nuclei for CO_2 ice, in agreement with the interpretation of heterogeneous over homogeneous nucleation (Määttänen et al., 2005)

but in disagreement with previous observations of iridescence in CO_2 ice clouds (e.g., Clancy et al., 2019). Based on the estimated particle sizes and abundances (Figure 3d), the number density of CO_2 ice particles is in the interval 0.01–2 cm^{-3}, consistent with previous works (e.g., Figure 18 in Clancy et al., 2019). However, the numerous caveats in the separation of different aerosols in SO data prevents from conclusively proving this point.

Dawn observations suggest a different scenario, where water ice particles may be the dominant condensation nuclei for CO_2. The two dawn cases are characterized by lower dust content, possibly due to diurnal variability in dust activity (Wolkenberg & Giuranna, 2021), while water ice is present from the lower atmosphere up to the same altitude as CO_2 ice. As seen in previous works (e.g., Liuzzi et al., 2020), generally water ice particle size decreases with altitude; here we see that small (<1.0 μm) ice particles are mixed with CO_2 ice, suggesting the former may act as condensation nuclei for the latter. At the altitudes where CO_2 ice is present, the density of water ice nuclei is 0.1–10 cm^{-3}, far larger than the CO_2 ice particle density (0.001–0.2 cm^{-3}); moreover, Figure 3e shows that the trend of the number density of smaller water ice nuclei is inconsistent with the constant-mass line of larger particles. Both considerations support the inference that part of the available water ice mass is trapped in CO_2 ice.

In most equatorial dusk cases (and in both the dawn observations) the highest CO_2 ice opacity is detected at or immediately below the altitude of CO_2 supersaturation, which could be interpreted as cloud formation being active at the time of those observations. The derived S peaks between 5 and >500 for dusk cases, and between 50 and 100 for dawn cases; the high S in some dusk cases is in agreement with the small particle size (and nuclei) observed, which requires high S to efficiently nucleate (Listowski et al., 2014). Aside from one case ($L_S = 120.2°$), the observation of CO_2 ice only in supersaturated regions seems consistent with the hypothesis that CO_2 ice sublimation is controlled by the cold pocket itself, rather than by the sedimentation of CO_2 ice out of the cold pocket where it forms (Listowski et al., 2014). SO observations do not disprove the idea that the observed cold pockets and CO_2 ice clouds (high S) may be the result of gravity wave activity, which at aphelion is mostly confined between 20 °S and 20 °N (Creasey et al., 2006).

3.3. Hellas Clouds at Dawn

CO_2 ice clouds in the Hellas region have been rarely reported in daytime observations. Ice clouds were first reported by MCS limb observations at 3 p.m. in band A6 (Sefton-Nash et al., 2013) and at 5–11 a.m. by IUVS (Stevens et al., 2017). Out of more than 20 SO occultations at dawn and dusk east of Hellas Basin at $L_S = 0–140°$, six of such clouds were detected in three temporal instances ($L_S = 53°, 103°, 121°$), and the first occurrence coincides geographically with one of the IUVS detections. These clouds are characterized by large CO_2 ice crystals (1–3 μm) between 40 and 60 km altitude, making them among the lowest CO_2 ice clouds observed (e.g., Määttänen et al., 2010). Yet it should be noted that a direct comparison with IUVS results is not possible, as IUVS altitudes were reported only when >60 km because of observational constraints. Dust is present from the surface to the bottom of the zone where CO_2 ice is seen, often with a vertical structure characterized by multiple layers, while water ice is scarce, if present at all. In all cases, the strongest constraint to identify the lowest altitude where CO_2 ice is located is the presence of the $\nu_1 + \nu_3$ feature in the data, which distinguishes dust from CO_2 ice. The continuity between the vertical distributions of CO_2 ice and dust suggests that the surface-lifted dust may provide most of the condensation nuclei for these clouds. The three instances where these clouds are seen may correspond to regional lifting of dust from Hellas Basin, seen also by MGS in Southern Winter (e.g., NASA/JPL/MSSS, 2001), and may fuel the formation of CO_2 ice clouds when sufficiently cold pockets occur in the mesosphere.

There are two explanations for these SO observations: either they show (a) ongoing sublimation, with CO_2 ice particles falling from the altitude where they formed, sublimating, and leaving dust nuclei visible; or (b) ongoing condensation, with dust being transported upwards and CO_2 condensing. The S inferred from the temperature proxy seems to favor hypothesis (a), as CO_2 ice appears in unsaturated air, indicating that ice could form before dawn in cold pockets that dissipate as the Sun rises. While providing a quantification of the lifetime of these clouds is beyond the scope of this work, we notice that the typical lifetime of CO_2 ice in unsaturated air is short (10–30 min, Listowski et al. (2014)). Precipitation from the formation zone may also play a role in their sublimation, as in the upper mesosphere micron-sized particles can precipitate by

several kilometers in minutes (Colaprete & Toon, 2003; Glandorf et al., 2002). In one profile (L_S = 102.8°) this argument appears to be true, with CO_2 ice particles increasing in radius as altitude decreases, even with thermal conditions far from saturation.

Despite the generally large particle size, Hellas dawn CO_2 ice particle number density is comparable to the Equatorial clouds, between 0.005-1 cm^{-3} (Figure 3f). If dust nuclei size are comparable to that of the CO_2 ice, this would not require very high S (Glandorf et al., 2002), consistent with SO observations. Nevertheless, high values of S (>500) are locally observed in the L_S = 53.1° case, where the CO_2 ice abundance could be as high as 4×10^{-4} kg/kg. Considering the lack of continuous temporal sampling and the sporadic frequency of SO detections of CO_2 ice clouds, these cases cannot be used to definitively distinguish whether the source of high-altitude nuclei are more widely available than surface-lifted dust or water ice, such as meteoric smoke (Clancy et al., 2019; Crismani et al., 2017; Hartwick et al., 2019; Plane et al., 2018) may provide the necessary nuclei to activate CO_2 condensation. More modeling studies and follow-up observations with TGO of these high-altitude clouds in connection with local aerosol lifting, gravity waves and thermal tides will be needed to provide more insights into their lifetime and frequency.

Data Availability Statement

The retrieval package used in this study is the Planetary Spectrum Generator, free and available online at https://psg.gsfc.nasa.gov/helpatm.php#retrieval, at the PSG GitHub site: https://github.com/nasapsg/retrievalOE. The data used in this analysis are available at https://nomad.aeronomie.be/index.php/data, while the data corresponding to the figures are available on Zenodo (Liuzzi, 2021).

Acknowledgments
ExoMars is a space mission of the European Space Agency (ESA) and Roscosmos. The NOMAD experiment is led by the Royal Belgian Institute for Space Aeronomy (IASB-BIRA), assisted by Co-PI teams from Spain (IAA-CSIC), Italy (INAF-IAPS), and the United Kingdom (Open University). This project acknowledges funding by the Belgian Science Policy Office (BELSPO), with the financial and contractual coordination by the ESA Prodex Office (PEA 4000103401, 4000121493), by the Spanish MICINN through its Plan Nacional and by European funds under grants PGC2018-101836-B-I00 and ESP2017-87143-R (MINECO/FEDER), as well as by UK Space Agency through grants ST/V002295/1, ST/V005332/1, ST/R001405/1 and ST/S00145X/1 and Italian Space Agency through grant 2018-2-HH.0. The IAA/CSIC team acknowledges financial support from the State Agency for Research of the Spanish MCIU through the "Center of Excellence Severo Ochoa" award for the Instituto de Astrofísica de Andalucía (SEV-2017-0709). This work was supported by NASA's Mars Program Office under WBS 604796, "Participation in the TGO/NOMAD Investigation of Trace Gases on Mars" and by NASA's SEEC initiative under Grant Number NNX17AH81A, "Remote sensing of Planetary Atmospheres in the Solar System and Beyond". This project has received funding from the European Union's Horizon 2020 research and innovation programme under grant agreement No. 101004052. U.S. investigators were supported by the National Aeronautics and Space Administration.

References

Aoki, S., Sato, Y., Giuranna, M., Wolkenberg, P., Sato, T. M., Nakagawa, H., & Kasaba, Y. (2018). Mesospheric CO_2 ice clouds on Mars observed by Planetary Fourier Spectrometer onboard Mars Express. *Icarus*, *302*, 175–190. https://doi.org/10.1016/j.icarus.2017.10.047

Clancy, R. T., Grossman, A. W., Wolff, M. J., James, P. B., Rudy, D. J., Billawala, Y. N., et al. (1996). Water vapor saturation at low altitudes around Mars Aphelion: A key to Mars climate? *Icarus*, *122*(1), 36–62. https://doi.org/10.1006/icar.1996.0108

Clancy, R. T., & Sandor, B. J. (1998). CO_2 ice clouds in the upper atmosphere of Mars. *Geophysical Research Letters*, *25*(4), 489–492. https://doi.org/10.1029/98GL00114

Clancy, R. T., Wolff, M., Whitney, B., & Cantor, B. (2004). The Distribution of High Altitude (70KM) Ice Clouds in the Mars Atmospere from MGS TES and MOC LIMB Observations. Presented at the Bulletin of the American Astronomical Society (Vol. *36*, 26.06).

Clancy, R. T., Wolff, M. J., Smith, M. D., Kleinböhl, A., Cantor, B. A., Murchie, S. L., et al. (2019). The distribution, composition, and particle properties of Mars mesospheric aerosols: An analysis of CRISM visible/near-IR limb spectra with context from near-coincident MCS and MARCI observations. *Icarus*, *328*, 246–273. https://doi.org/10.1016/j.icarus.2019.03.025

Clancy, R. T., Wolff, M. J., Whitney, B. A., Cantor, B. A., & Smith, M. D. (2007). Mars equatorial mesospheric clouds: Global occurrence and physical properties from Mars Global Surveyor Thermal Emission Spectrometer and Mars Orbiter Camera limb observations. *Journal of Geophysical Research*, *112*(E4), E04004. https://doi.org/10.1029/2006JE002805

Colaprete, A., & Toon, O. B. (2003). Carbon dioxide clouds in an early dense Martian atmosphere. *Journal of Geophysical Research*, *108*(E4), 5025. https://doi.org/10.1029/2002JE001967

Creasey, J. E., Forbes, J. M., & Keating, G. M. (2006). Density variability at scales typical of gravity waves observed in Mars' thermosphere by the MGS accelerometer. *Geophysical Research Letters*, *33*(22), L22814. https://doi.org/10.1029/2006GL027583

Crismani, M. M. J., Schneider, N. M., Plane, J. M. C., Evans, J. S., Jain, S. K., Chaffin, M. S., et al. (2017). Detection of a persistent meteoric metal layer in the Martian atmosphere. *Nature Geoscience*, *10*(6), 401–404. https://doi.org/10.1038/ngeo2958

Glandorf, D. L., Colaprete, A., Tolbert, M. A., & Toon, O. B. (2002). CO_2 snow on Mars and early Earth: Experimental constraints. *Icarus*, *160*(1), 66–72. https://doi.org/10.1006/icar.2002.6953

González-Galindo, F., Määttänen, A., Forget, F., & Spiga, A. (2011). The martian mesosphere as revealed by CO_2 cloud observations and general circulation modeling. *Icarus*, *216*(1), 10–22. https://doi.org/10.1016/j.icarus.2011.08.006

Hartwick, V. L., Toon, O. B., & Heavens, N. G. (2019). High-altitude water ice cloud formation on Mars controlled by interplanetary dust particles. *Nature Geoscience*, *12*(7), 516–521. https://doi.org/10.1038/s41561-019-0379-6

Jiang, F. Y., Yelle, R. V., Jain, S. K., Cui, J., Montmessin, F., Schneider, N. M., et al. (2019). Detection of mesospheric CO_2 ice clouds on Mars in southern summer. *Geophysical Research Letters*, *46*(14), 7962–7971. https://doi.org/10.1029/2019GL082029

Kasting, J. F. (1991). CO_2 condensation and the climate of early Mars. *Icarus*, *94*(1), 1–13. https://doi.org/10.1016/0019-1035(91)90137-I

Listowski, C., Määttänen, A., Montmessin, F., Spiga, A., & Lefèvre, F. (2014). Modeling the microphysics of CO_2 ice clouds within wave-induced cold pockets in the martian mesosphere. *Icarus*, *237*, 239–261. https://doi.org/10.1016/j.icarus.2014.04.022

Liuzzi, G. (2021). Data in support of the publication "First Detection and Thermal Characterization of Terminator CO_2 Ice Clouds with ExoMars/NOMAD" on Geophysical Research Letters. https://doi.org/10.5281/zenodo.5572859

Liuzzi, G., Masiello, G., Serio, C., Venafra, S., & Camy-Peyret, C. (2016). Physical inversion of the full IASI spectra: Assessment of atmospheric parameters retrievals, consistency of spectroscopy and forward modelling. *Journal of Quantitative Spectroscopy and Radiative Transfer*, *182*, 128–157. https://doi.org/10.1016/j.jqsrt.2016.05.022

Liuzzi, G., Villanueva, G. L., Crismani, M. M. J., Smith, M. D., Mumma, M. J., Daerden, F., et al. (2020). Strong variability of Martian water ice clouds during dust storms revealed from ExoMars trace gas orbiter/NOMAD. *Journal of Geophysical Research*, *125*(4), e2019JE006250. https://doi.org/10.1029/2019JE006250

Liuzzi, G., Villanueva, G. L., Mumma, M. J., Smith, M. D., Daerden, F., Ristic, B., et al. (2019). Methane on Mars: New insights into the sensitivity of CH_4 with the NOMAD/ExoMars spectrometer through its first in-flight calibration. *Icarus*, *321*, 671–690. https://doi.org/10.1016/j.icarus.2018.09.021

Määttänen, A., Montmessin, F., Gondet, B., Scholten, F., Hoffmann, H., González-Galindo, F., et al. (2010). Mapping the mesospheric CO_2 clouds on Mars: MEx/OMEGA and MEx/HRSC observations and challenges for atmospheric models. *Icarus*, *209*(2), 452–469. https://doi.org/10.1016/j.icarus.2010.05.017

Määttänen, A., Vehkamäki, H., Lauri, A., Merikallio, S., Kauhanen, J., Savijärvi, H., & Kulmala, M. (2005). Nucleation studies in the Martian atmosphere. *Journal of Geophysical Research*, *110*(E2), E02002. https://doi.org/10.1029/2004JE002308

Magalhães, J. A., Schofield, J. T., & Seiff, A. (1999). Results of the Mars pathfinder atmospheric structure investigation. *Journal of Geophysical Research*, *104*(E4), 8943–8955. https://doi.org/10.1029/1998JE900041

Mahieux, A., Vandaele, A. C., Robert, S., Wilquet, V., Drummond, R., López Valverde, M. A., et al. (2015). Rotational temperatures of Venus upper atmosphere as measured by SOIR on board Venus Express. *Planetary and Space Science*, *113–114*, 347–358. https://doi.org/10.1016/j.pss.2014.12.020

McCleese, D. J., Heavens, N. G., Schofield, J. T., Abdou, W. A., Bandfield, J. L., Calcutt, S. B., et al. (2010). Structure and dynamics of the Martian lower and middle atmosphere as observed by the Mars climate sounder: Seasonal variations in zonal mean temperature, dust, and water ice aerosols. *Journal of Geophysical Research*, *115*(E12), E12016. https://doi.org/10.1029/2010JE003677

Millour, E., Forget, F., Spiga, A., Navarro, T., Madeleine, J.-B., Montabone, L., et al. (2015). The Mars climate database (MCD version 5.2). *European Planetary Science Congress*, *10*, EPSC2015–438.

Montmessin, F., Bertaux, J.-L., Quémerais, E., Korablev, O., Rannou, P., Forget, F., et al. (2006). Subvisible CO_2 ice clouds detected in the mesosphere of Mars. *Icarus*, *183*(2), 403–410. https://doi.org/10.1016/j.icarus.2006.03.015

Montmessin, F., Gondet, B., Bibring, J.-P., Langevin, Y., Drossart, P., Forget, F., & Fouchet, T. (2007). Hyperspectral imaging of convective CO_2 ice clouds in the equatorial mesosphere of Mars. *Journal of Geophysical Research*, *112*(E11), E11S90. https://doi.org/10.1029/2007JE002944

NASA/JPL/MSSS. (2001). "*Mid Winter Dust Storms Near Hellas Planitia*". Retrieved from https://www.jpl.nasa.gov/spaceimages/details.php?id=PIA03222

Neary, L., & Daerden, F. (2018). The GEM-Mars general circulation model for Mars: Description and evaluation. *Icarus*, *300*, 458–476. https://doi.org/10.1016/j.icarus.2017.09.028

Neefs, E., Vandaele, A. C., Drummond, R., Thomas, I. R., Berkenbosch, S., Clairquin, R., et al. (2015). NOMAD spectrometer on the ExoMars trace gas orbiter mission: Part 1—Design, manufacturing and testing of the infrared channels. *Applied Optics*, *54*(28), 8494. https://doi.org/10.1364/AO.54.008494

Noguchi, K., Ikeda, S., Kuroda, T., Tellmann, S., & Pätzold, M. (2014). Estimation of changes in the composition of the Martian atmosphere caused by CO_2 condensation from GRS Ar measurements and its application to the rederivation of MGS radio occultation measurements. *Journal of Geophysical Research: Planets*, *119*(12), 2510–2521. https://doi.org/10.1002/2014JE004629

Piccialli, A., López-Valverde, M. A., Määttänen, A., González-Galindo, F., Audouard, J., Altieri, F., et al. (2016). CO_2 non-LTE limb emissions in Mars' atmosphere as observed by OMEGA/Mars Express. *Journal of Geophysical Research: Planets*, *121*(6), 1066–1086. https://doi.org/10.1002/2015JE004981

Plane, J. M. C., Carrillo-Sanchez, J. D., Mangan, T. P., Crismani, M. M. J., Schneider, N. M., & Määttänen, A. (2018). Meteoric metal chemistry in the Martian atmosphere. *Journal of Geophysical Research: Planets*, *123*(3), 695–707. https://doi.org/10.1002/2017JE005510

Rodgers, C. D. (2000). *Inverse methods for atmospheric sounding | series on atmospheric, oceanic and planetary physics*. Retrievedfrom https://www.worldscientific.com/worldscibooks/10.1142/3171

Sánchez-Lavega, A., Muñoz, A. G., García-Melendo, E., Pérez-Hoyos, S., Gómez-Forrellad, J. M., Pellier, C., et al. (2015). An extremely high-altitude plume seen at Mars' morning terminator. *Nature*, *518*(7540), 525–528. https://doi.org/10.1038/nature14162

Sánchez-Lavega, A., Pérez-Hoyos, S., & Hueso, R. (2004). Clouds in planetary atmospheres: A useful application of the Clausius–Clapeyron equation. *American Journal of Physics*, *72*(6), 767–774. https://doi.org/10.1119/1.1645279

Schofield, J. T., Barnes, J. R., Crisp, D., Haberle, R. M., Larsen, S., Magalhães, J. A., et al. (1997). The Mars pathfinder atmospheric structure investigation/meteorology (ASI/MET) experiment. *Science*, *278*(5344), 1752–1758. https://doi.org/10.1126/science.278.5344.1752

Sefton-Nash, E., Teanby, N. A., Montabone, L., Irwin, P. G. J., Hurley, J., & Calcutt, S. B. (2013). Climatology and first-order composition estimates of mesospheric clouds from Mars climate sounder limb spectra. *Icarus*, *222*(1), 342–356. https://doi.org/10.1016/j.icarus.2012.11.012

Smith, M. D. (2004). Interannual variability in TES atmospheric observations of Mars during 1999–2003. *Icarus*, *167*(1), 148–165. https://doi.org/10.1016/j.icarus.2003.09.010

Smith, M. D., Wolff, M. J., Clancy, R. T., Kleinböhl, A., & Murchie, S. L. (2013). Vertical distribution of dust and water ice aerosols from CRISM limb-geometry observations. *Journal of Geophysical Research: Planets*, *118*(2), 321–334. https://doi.org/10.1002/jgre.20047

Spiga, A., Faure, J., Madeleine, J.-B., Määttänen, A., & Forget, F. (2013). Rocket dust storms and detached dust layers in the Martian atmosphere. *Journal of Geophysical Research: Planets*, *118*(4), 746–767. https://doi.org/10.1002/jgre.20046

Spiga, A., González-Galindo, F., López-Valverde, M.-Á., & Forget, F. (2012). Gravity waves, cold pockets and CO_2 clouds in the Martian mesosphere. *Geophysical Research Letters*, *39*(2), L02201. https://doi.org/10.1029/2011GL050343

Stevens, M. H., Siskind, D. E., Evans, J. S., Jain, S. K., Schneider, N. M., Deighan, J., et al. (2017). Martian mesospheric cloud observations by IUVS on MAVEN: Thermal tides coupled to the upper atmosphere. *Geophysical Research Letters*, *44*(10), 4709–4715. https://doi.org/10.1002/2017GL072717

Thomas, I. R., Vandaele, A. C., Robert, S., Neefs, E., Drummond, R., Daerden, F., et al. (2016). Optical and radiometric models of the NOMAD instrument part II: The infrared channels - SO and LNO. *Optics Express*, *24*(4), 3790. https://doi.org/10.1364/OE.24.003790

Vandaele, A. C., Lopez-Moreno, J.-J., Patel, M. R., Bellucci, G., Daerden, F., Ristic, B., et al. (2018). NOMAD, an integrated suite of three spectrometers for the ExoMars trace gas mission: Technical description, science objectives and expected performance. *Space Science Reviews*, *214*(5), 80. https://doi.org/10.1007/s11214-018-0517-2

Villanueva, G. L., Smith, M. D., Protopapa, S., Faggi, S., & Mandell, A. M. (2018). Planetary spectrum generator: An accurate online radiative transfer suite for atmospheres, comets, small bodies and exoplanets. *Journal of Quantitative Spectroscopy and Radiative Transfer*, *217*, 86–104. https://doi.org/10.1016/j.jqsrt.2018.05.023

Vincendon, M., Pilorget, C., Gondet, B., Murchie, S., & Bibring, J.-P. (2011). New near-IR observations of mesospheric CO_2 and H_2O clouds on Mars. *Journal of Geophysical Research*, *116*(E11), E00J02. https://doi.org/10.1029/2011JE003827

Warren, S. G. (1986). Optical constants of carbon dioxide ice. *Applied Optics*, *25*(16), 2650–2674. https://doi.org/10.1364/AO.25.002650

Wolff, M. J., Clancy, R. T., Kahre, M. A., Haberle, R. M., Forget, F., Cantor, B. A., & Malin, M. C. (2019). Mapping water ice clouds on Mars with MRO/MARCI. *Icarus*, *332*, 24–49. https://doi.org/10.1016/j.icarus.2019.05.041

Wolkenberg, P., & Giuranna, M. (2021). Daily dust variation from the PFS MEx observations. *Icarus*, *353*, 113823. https://doi.org/10.1016/j.icarus.2020.113823

Wood, B. E., & Roux, J. A. (1982). Infrared optical properties of thin H_2O, NH_3, and CO_2 cryofilms. *JOSA*, *72*(6), 720–728. https://doi.org/10.1364/JOSA.72.000720

Yiğit, E., Medvedev, A. S., & Hartogh, P. (2015). Gravity waves and high-altitude CO_2 ice cloud formation in the Martian atmosphere. *Geophysical Research Letters*, *42*(11), 4294–4300. https://doi.org/10.1002/2015GL064275

References From the Supporting Information

Aoki, S., Vandaele, A. C., Daerden, F., Villanueva, G. L., Liuzzi, G., Thomas, I. R., et al. (2019). Water vapor vertical profiles on Mars in dust storms observed by TGO/NOMAD. *Journal of Geophysical Research: Planets*, *124*(12), 3482–3497. https://doi.org/10.1029/2019JE006109

Carissimo, A., De Feis, I., & Serio, C. (2005). The physical retrieval methodology for IASI: The δ-IASI code. *Environmental Modelling & Software*, *20*(9), 1111–1126. https://doi.org/10.1016/j.envsoft.2004.07.003

Isokoski, K., Poteet, C. A., & Linnartz, H. (2013). Highly resolved infrared spectra of pure CO_2 ice (15–75 K). *Astronomy & Astrophysics*, *555*, A85. https://doi.org/10.1051/0004-6361/201321517

Masiello, G., Serio, C., Carissimo, A., Grieco, G., & Matricardi, M. (2009). Application of φ-IASI to IASI: Retrieval products evaluation and radiative transfer consistency. *Atmospheric Chemistry and Physics*, *9*(22), 8771–8783.

Nevejans, D., Neefs, E., Van Ransbeeck, E., Berkenbosch, S., Clairquin, R., De Vos, L., et al. (2006). Compact high-resolution spaceborne echelle grating spectrometer with acousto-optical tunable filter based order sorting for the infrared domain from 2.2 to 4.3 μm. *Applied Optics*, *45*(21), 5191–5206.

Quémerais, E., Bertaux, J.-L., Korablev, O., Dimarellis, E., Cot, C., Sandel, B. R., & Fussen, D. (2006). Stellar occultations observed by SPICAM on Mars Express. *Journal of Geophysical Research*, *111*(E9), E09S04. https://doi.org/10.1029/2005JE002604

Villanueva, G. L., Liuzzi, G., Crismani, M. M. J., Aoki, S., Vandaele, A. C., Daerden, F., et al. (2021). Water heavily fractionated as it ascends on Mars as revealed by ExoMars/NOMAD. *Science Advances*, *7*(7), eabc8843. https://doi.org/10.1126/sciadv.abc8843